Pergamon

Int. J. Heat Mass Transfer. Vol. 37, No. 3, pp. 401–409, 1994

0017-9310/94 $6.00+0.00

Conjugate analysis of a flat-plate type evaporator for capillary pumped loops with three-dimensional vapor flow in the groove

YIDING CAO and AMIR FAGHRI

Department of Mechanical and Materials Engineering, Wright State University, Dayton, OH 45435, U.S.A.

(*Received* 10 *February* 1993 *and in final form* 27 *July* 1993)

Abstract—The physical operational mechanisms for the evaporator of capillary pumped loops are described, and possible working limits are identified. A generalized mathematical formulation for the flat-plate type evaporator is given, which includes liquid flow and heat transfer in the porous wick structure, three-dimensional vapor flow in the groove, and heat transfer in the cover plate. The liquid and vapor flows are coupled via the interfacial mass flux, and the entire evaporator is solved as a conjugate problem. Numerical results under different working conditions and with different fluids are presented, which provide guidance for the evaporator design of capillary pumped loops.

INTRODUCTION

DUE TO high power thermal transport requirements for many proposed space-based systems, the capillary pumped loop (CPL) has been developed, and has become a candidate for the thermal management system of spacecraft with high power loads (Chalmers *et al.* [1], Ku *et al.* [2], Holmes *et al.* [3]). In heat pipes, the capillary force provides the necessary pumping pressure to return the liquid condensate to the evaporator from the condenser. Since the capillary force available in a heat pipe is limited, the power loads and heat transfer distance often suffer serious restraints because of the large liquid flow resistance in the wick. The CPL, however, is a continuous loop with vapor and liquid flowing in the same direction. Unlike the heat pipe, the CPL requires a wick structure only in the evaporator section, and the pressure losses in the CPL are significantly reduced compared to those in the heat pipe. As a result, a large increase in the thermal transport capacity is possible over that seen with heat pipes. A generic capillary pumped loop is schematically shown in Fig. 1.

Most CPL designs consist of an evaporator, a condenser, a two-phase reservoir, and connecting plumbing [2, 4, 5]. Some of the designs also include mechanical pumps in the loop [6]. In capillary pumped loops, the evaporator design is crucial to the heat transfer performance. A typical plate-type capillary evaporator consists of a liquid flow passage, a porous wick structure, and a cover plate to which a heater is attached [7, 8]. The bottom of the cover plate is provided with fins which are in contact with the wick structure. The heat flows from the heater to the liquid–vapor interface in a direction opposite to that of the capillary liquid movement, and evaporates into the grooves formed between fins. The vapor flows through the grooves into the transverse vapor-collecting channels, and from there to the vapor duct. The evaporator is the most important part of the capillary pumped loop, which needs specific consideration. Wulz and Embacher [8] modeled a flat-plate type evaporator using a steady state two-dimensional model. The evaporation location of the liquid–vapor interface and the interface temperature were prescribed, which are generally unknown, and liquid flow and heat transfer in the wick region were considered.

In the present paper, the physical operational mechanisms of the CPL evaporator are described, and a general model which couples the liquid flow in the wick and three-dimensional vapor flow in the grooves is proposed. The model is also capable of simulating the transient heat transfer and fluid flow processes in the CPL evaporator. To the authors' knowledge, these issues have not been addressed completely before.

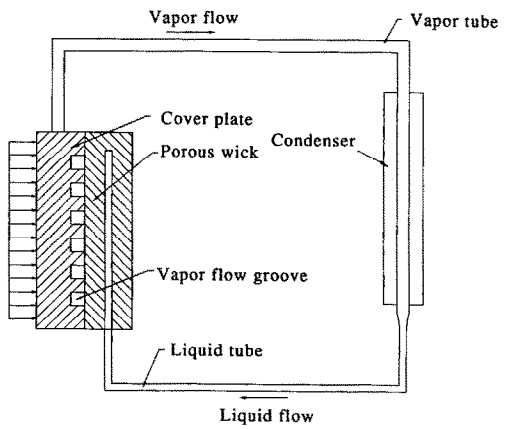

FIG. 1. Schematic of a generic capillary pumped loop.

NOMENCLATURE

c_p	specific heat [J kg^{-1} K^{-1}]
h_{fg}	latent heat of evaporation [J kg^{-1}]
k	thermal conductivity [W m^{-1} K^{-1}]
K	wick permeability [m^2]
L_x	total length in x direction [m]
L_y	total length in y direction [m]
L_z	total length in z direction [m]
L_{xf}	heated length in the x direction [m]
L_{yf}	height of the upper surface of the groove [m]
L_{yw}	height of the porous structure [m]
$\dot{m}_\delta$	vapor mass flux due to evaporation [kg m^{-2} s^{-1}]
p	pressure [N m^{-2}]
q	heat flux [W m^{-2}]
R_g	gas constant [J kg^{-1} K^{-1}]
r	effective capillary radius of the wick pores [m]
T	temperature [K]
t	time [s]
u	velocity in x direction [m s^{-1}]
$\mathbf{V}$	velocity vector [m s^{-1}]
v	velocity in y direction [m s^{-1}]
v_{in}	liquid velocity at $y = 0$ [m s^{-1}]
$v_{l,\delta}$	liquid velocity at liquid–vapor interface [m s^{-1}]
$v_{v,\delta}$	vapor velocity at liquid–vapor interface [m s^{-1}]
w	velocity in z direction [m s^{-1}]
x, y, z	coordinates [m].

Greek symbols

α	thermal diffusivity [m^2 s^{-1}]
β	accommodation coefficient
θ	effective contact angle
μ	viscosity [Pa s]
ρ	density [kg m^{-3}]
σ	liquid–vapor surface tension [N m^{-1}]
φ	porosity.

Subscripts

c	condenser
co	cover plate
e	evaporator
eff	effective
in	inlet
l	liquid
min	minimum
out	outlet at $z = L_z$
rf	reference
s	solid structure
v	vapor
δ	liquid–vapor interface.

OPERATION OF THE CPL EVAPORATOR

Due to symmetry, a segment cut out of a flat-plated evaporator is studied. The cut was made through the axes of the fin and the adjacent groove. Such a segment is schematically shown in Fig. 2.

The pumping force for the CPL evaporator is provided by the pressure head developed at the liquid–vapor interface

$$\Delta p = p_v - p_l = \frac{2\sigma\cos\theta}{r} \tag{1}$$

where σ is the liquid–vapor surface tension, θ is the effective or average contact angle, and r is the effective radius of the wick pores at the interface. The effective contact angle θ in equation (1) should be considered to be the dynamic contact angle instead of the static one, and its value changes during transient operation.

Before the CPL startup, no heat is applied at the evaporator, and the CPL evaporator is under thermal and mechanical equilibrium, $\Delta p = 0$. The contact angle in this case should be $\pi/2$, which means that the pores at the liquid–vapor interface are flooded by the liquid. A cross section of the segment in Fig. 2 at this condition is schematically shown in Fig. 3(a).

At time $t = 0$, heat is applied at the CPL evaporator, which is transferred through the fin and reaches the liquid–vapor interface. Evaporation takes place at the interface, and vapor flows into the groove. As a result, the liquid is drawn through the wick to the liquid–vapor interface to preserve the mass balance. At the same time, capillary menisci are established at the interface with an effective contact angle θ. These menisci facilitate the pumping function, which draws liquid from the wick to the liquid–vapor interface and circulates the fluid throughout the CPL. If the power load is increased at the evaporator, the effective con-

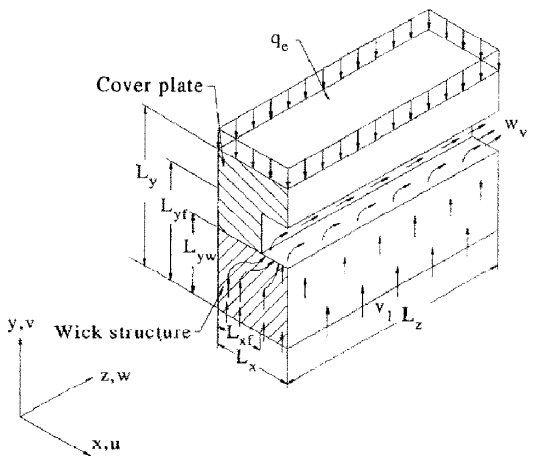

FIG. 2. Schematic of the modeled CPL evaporator segment.

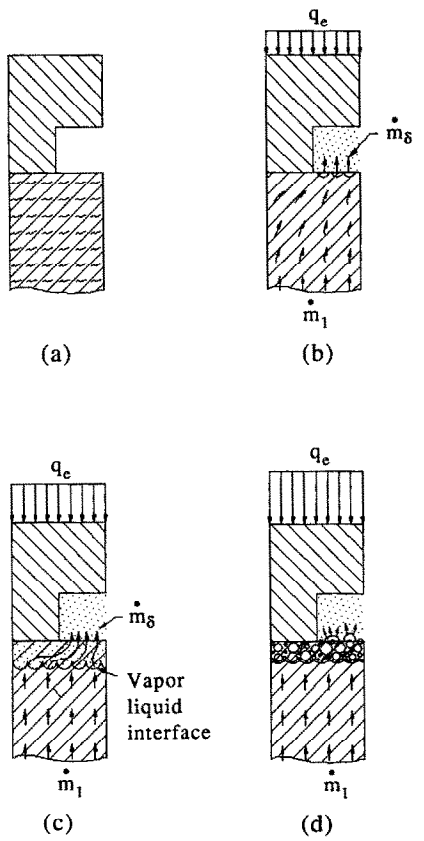

FIG. 3. Description of different operating conditions for a CPL evaporator.

tact angle θ will decrease, resulting in an increase of the capillary pumping head and a higher liquid flow rate. This operating condition is shown schematically in Fig. 3(b).

As the power load at the evaporator is further increased, the effective contact angle will reach a limit θ_{min}, and the capillary pumping head will reach a maximum. In this case, the liquid interface will recede into the wick to reduce the liquid flow resistance in the wick structure. This operating condition is shown schematically in Fig. 3(c). The pressure balance for the whole CPL at the steady state is

$$\frac{2\sigma\cos\theta}{r} = \Delta p_{l,e} + \Delta p_{v,e} + \Delta p_v + \Delta p_c + \Delta p_l \quad (2)$$

where $\Delta p_{l,e}$ is the pressure drop due to the liquid flow in the wick structure of the evaporator, $\Delta p_{v,e}$ is the pressure drop due to vapor flow in grooves, Δp_v is the pressure drop due to vapor flow in the pipeline between the evaporator and the condenser, Δp_c is the pressure drop in the condenser, and Δp_l is the pressure drop due to the liquid flow in the pipeline between the condenser and the evaporator. Since the height of the wick structure is small (usually on the order of a millimeter), the liquid pressure drop in the evaporator wick structure should be very small. As a result, the capillary limit at the operating condition shown in Fig. 3(c) has been already reached. Therefore, this operating condition should be avoided when designing a CPL evaporator if the capillary force is the only driving force for the CPL operation.

Since heat is transferred from the cover plate fin to the liquid–vapor interface, a temperature gradient is established at the fin–wick interface. When the heat flux is high, boiling may begin at the fin–wick interface. If the number and the size of vapor bubbles generated at the interface are small, these bubbles may migrate from the fin–wick interface to the liquid–vapor interface, and vent into the vapor groove without destroying the capillary menisci. However, as the heat flux is increased further, bubbles generated may coalesce, form a vapor blanket at the fin–wick interface, and be released into the groove with a high pulsive vapor pressure. In this case, the capillary menisci at the liquid–vapor interface will be destroyed and the boiling limit will be reached. This boiling limit is very similar to that of the conventional heat pipe in which the capillary pumping force is eliminated due to the destruction of the capillary menisci. The working condition in this case is schematically shown in Fig. 3(d). Like the working condition in Fig. 3(c), a two-phase reservoir or mechanical pump is needed to maintain the operation of the CPL. The operating condition shown in Fig. 3(b), on the other hand, is the normal operating condition for a CPL evaporator without the assistance of a mechanical pump or two-phase reservoir. For this reason, the operating condition shown in Fig. 3(b) is modeled in this paper for the purpose of CPL design.

MATHEMATICAL FORMULATION

For the flow and heat transfer in the porous wick structure, the wick is assumed to be homogeneous and isotropic, where the volume-averaged technique is applied. For an incompressible fluid, the continuity and momentum equations can be written as [9]

$$\frac{\partial u_i}{\partial x_i} = 0 \quad (3)$$

$$\frac{\rho}{\varphi}\left(\frac{\partial u_i}{\partial t} + \frac{1}{\varphi}\mathbf{V}\cdot\nabla u_i\right) = -\frac{\partial p}{\partial x_i} + \frac{\mu}{\varphi}\nabla^2 u_i - \frac{\mu}{K}u_i \quad (4)$$

$$(i = 1, 2, 3)$$

where x_1, x_2 and x_3 correspond to x, y, and z respectively; u_1, u_2 and u_3 correspond to u, v, and w, φ is the porosity of the wick, and K is the wick permeability.

The continuity and momentum equations for the vapor flow in the groove, under the condition of varying density but constant viscosity μ, are [10]

$$\frac{\partial \rho}{\partial t} + \rho\nabla\cdot\mathbf{V} = 0 \quad (5)$$

$$\rho\frac{\mathrm{D}\mathbf{V}}{\mathrm{D}t} = -\nabla p + \frac{1}{3}\mu\nabla(\nabla\cdot\mathbf{V}) + \mu\nabla^2\mathbf{V}. \quad (6)$$

The equation of state is given by

$$p = \rho R_g T. \quad (7)$$

The energy equation for the whole CPL evaporator can be generally written as [11]

$$\omega\frac{\partial T}{\partial t} + \mathbf{V}\cdot\nabla T = \alpha\nabla^2 T \quad (8)$$

where

$$\omega = \frac{\varphi\rho_j c_{p,j} + (1-\varphi)\rho_s c_{p,s}}{\rho_j c_{p,j}},$$

$$\alpha = \frac{k_{\mathrm{eff},j}}{\rho_j c_{p,j}} = \frac{\varphi k_j + (1-\varphi)k_s}{\rho_j c_{p,j}}.$$

The subscript j refers to the three regions of interest: the solid cover plate, the wick, and the vapor space.

In the cover plate region, heat transfer is purely by conduction

$$\varphi \equiv 0, \quad \mathbf{V} \equiv 0$$

$$\rho_j c_{p,j} = \rho_s c_{p,s} = \rho_{co} c_{p,co}, \quad k_j = k_s = k_{co}. \quad (9)$$

It follows that,

$$\omega \equiv 1, \quad \alpha = k_{co}/\rho_{co} c_{p,co}.$$

In the groove region,

$$\varphi \equiv 1, \quad \rho_j c_{p,j} = \rho_v c_{p,v}, \quad k_j = k_v. \quad (10)$$

Therefore,

$$\omega \equiv 1, \quad \alpha = k_v/\rho_v c_{p,v}.$$

In the wick structure region,

$$\rho_j c_{p,j} = \rho_l c_{p,l}, \quad k_j = k_l. \quad (11)$$

For the analysis presented in this paper, the heat transfer in the three regions is coupled, and the conservation equations are solved as a conjugate problem. The boundary conditions are described below.

At $x = 0$ and $x = L_x$,

$$u = 0, \quad \frac{\partial v}{\partial x} = 0, \quad \frac{\partial w}{\partial x} = 0, \quad \frac{\partial T}{\partial x} = 0. \quad (12)$$

At $y = L_y$,

$$k_{co}\frac{\partial T}{\partial y} = q_e. \quad (13)$$

At $y = 0$,

$$u = w = 0, \quad \frac{\partial v}{\partial y} = 0, \quad T = T_{in}. \quad (14)$$

At $z = 0$,

$$w = u = v = 0, \quad \frac{\partial T}{\partial z} = 0. \quad (15)$$

At $z = L_z$,

$$\frac{\partial w}{\partial z} = 0, \quad u = v = 0, \quad \frac{\partial T}{\partial z} = 0. \quad (16)$$

The boundary condition at the liquid–vapor interface is more involved. The liquid–vapor interface ($y = L_{yw}$ and $L_{xf} < x < L_x$) is assumed to be flat. A mass flux $\dot{m}_\delta$ due to the evaporation into the groove needs to be calculated. The liquid velocity at the interface on the wick side is $v_{l,\delta} = \dot{m}_\delta/\rho_l$, and the corresponding interface vapor velocity on the vapor side is $v_{v,\delta} = \dot{m}_\delta/\rho_v$. For the calculation of heat transfer, the two regions are solved as a conjugate problem, and $\dot{m}_\delta$ is directly used in the energy equation at the interface. In addition, a heat sink, $\dot{m}_\delta h_{fg}$, is applied at the grids on the wick region side next to the interface to simulate the latent heat absorption due to evaporation. The thermal conductivities for both regions at the interface are

$$k_\delta = \frac{2k_v k_{\mathrm{eff}}}{k_v + k_{\mathrm{eff}}} \quad (17)$$

where k_{eff} is the effective thermal conductivity of the wick structure.

The mass flux can be calculated by the relation due to Silver and Simpson [12]

$$\dot{m}_\delta = \frac{2\beta}{2-\beta}\sqrt{\left(\frac{1}{2\pi R_g}\right)}\left(\frac{p_l^*}{\sqrt{T_l}} - \frac{p_v}{\sqrt{T_v}}\right) \quad (18)$$

where β is the accommodation coefficient. p_l^* is the equilibrium saturation pressure corresponding to the interfacial liquid temperature T_l, and can be calculated using the Clausius–Clapeyron equation

$$p_l^* = p_{rf}\exp\left[-\frac{h_{fg}}{R_g}\left(\frac{1}{T_l} - \frac{1}{T_{rf}}\right)\right] \quad (19)$$

where p_{rf} and T_{rf} are the reference pressure and temperature.

At the interfaces between the vapor and the cover plate ($x = L_{xf}$ and $L_{yw} < y < L_{yf}$; $y = L_{yf}$ and $L_{xf} < x < L_x$), $u = v = w = 0$ due to the no-slip condition. The heat transfer boundary condition can be written as

$$\left(k_{cv}\frac{\partial T}{\partial n}\right)_{co} = \left(k_{cv}\frac{\partial T}{\partial n}\right)_v \quad (20)$$

where the interface thermal conductivity is $k_{cv} = 2k_v k_{co}/(k_v + k_{co})$, and n is the direction normal to the cover–vapor interface.

NUMERICAL PROCEDURE

The conservation equations and boundary conditions were solved by applying the control volume based finite-difference method [13]. The three-dimen-

sional vapor flow in the groove was solved by using the partially-parabolic numerical procedure described by Pratap and Spalding [14], in which the second derivatives of the velocities in the z direction were neglected. The finite difference equations were solved by marching downstream. At each cross section, a two-dimensional elliptic flow was solved. The stepwise march was continued until the end of the flow domain was reached. The marching was repeated until a converged solution was obtained. For the liquid flow in the wick structure, the flow is predominantly in the x–y plane due to the heat input condition shown in Fig. 2. The liquid velocity in the z direction is negligibly small compared to u and v, and therefore was set to zero in the numerical computation. A combination of the direct method (TDMA) and the Gauss–Seidel method was employed to solve the discretization equation. The overall numerical sequence is as follows:

1. Initialize the numerical domain. For the case of evaporator startup, the initial vapor and liquid velocities are zero, and the initial temperature is uniform at T_{in}.
2. Calculate the liquid–vapor interface mass flux as well as the corresponding liquid and vapor interface velocities using equations (18) and (19).
3. Solve the three-dimensional vapor velocities in the groove region using equations (5)–(7) by the partially-parabolic method.
4. Solve the liquid flow in the porous wick structure region (equations (3) and (4)).
5. Solve the energy equations (8)–(11), over the whole evaporator domain. The three regions (cover plate, porous wick structure, and groove) are solved as a conjugate problem.
6. Go back to step 2 until the converged solution is obtained for each time step.

Grid independence has been studied, and it was found that the computer code written is essentially independent of the number of cells used. A change of the number of cells from $6(x)\times 9(y)\times 10(z)$ to $8(x)\times 13(y)\times 14(z)$ resulted in a maximum outer cover temperature change from 307.0 to 306.43 K. A further refinement to $12(x)\times 18(y)\times 20(z)$ gave a maximum temperature of 306.08 K. Although a numerical solution using finer grid gives a more accurate solution, the CPU time required is much higher due to the three-dimensional nature of this study. Therefore, most of the results in this study were obtained using a mesh of $8(x)\times 13(y)\times 14(z)$. The numerical model is also insensitive to the accommodation coefficient β. A change of β from $\beta = 0.1$ to 0.3 resulted in a change in the maximum temperature of less than 0.1%.

RESULTS AND DISCUSSION

For validation, the numerical model was examined by checking the overall mass and energy balances over the numerical domain. At the steady state, mass balances for liquid flow in the porous wick and vapor flow in the groove are given by the following expressions

$$\int_0^{L_x}\int_0^{L_z}\rho_l v_{in}\,dx\,dz=\int_{L_{xf}}^{L_x}\int_0^{L_z}\rho_l v_{l,\delta}\,dx\,dz \quad (21)$$

$$\int_{L_{xf}}^{L_x}\int_0^{L_z}\rho_v v_{v,\delta}\,dx\,dz=\int_{L_{xf}}^{L_x}\int_{L_{yw}}^{L_{yf}}(\rho_v w_v)_{out}\,dx\,dy \quad (22)$$

where v_{in} is the incoming liquid velocity at $y = 0$, $v_{l,\delta}$ is the liquid velocity at the liquid–vapor interface ($y = L_{yw}$, $L_{xf} < x < L_x$), $v_{v,\delta}$ is the corresponding vapor velocity at the interface, and $(\rho_v w_v)_{out}$ is the outflow vapor mass flux at $z = L_z$.

An energy balance over the numerical domain requires that

$$\int_0^{L_x}\int_0^{L_z}q_e\,dx\,dz+\int_0^{L_x}\int_0^{L_z}\left(-k_{eff}\left.\frac{\partial T}{\partial y}\right|_{y=0}\right)dx\,dz$$

$$=\int_{L_{xf}}^{L_x}\int_{L_{yw}}^{L_{yf}}(\rho_v w_v)_{out}[h_{fg}+c_p(T_{out}-T_{in})]\,dx\,dy. \quad (23)$$

The steady-state numerical results show that the equations above were satisfied with a maximum relative error of 1 to 2%.

Numerical computations were first made with Freon-11 as the working fluid. The thermal properties taken in the computation are: $c_p = 1.02\times 10^3$ J kg^{-1} K^{-1}, $k_l = 0.084$ W m^{-1} K^{-1}, $\rho_l = 1440$ kg m^{-3}, and $h_{fg} = 1.756\times 10^5$ J kg^{-1}. The properties for the wick structure are: $K = 10^{-11}$ m^2, $k_s = 10$ W m^{-1} K^{-1}, $c_{p,s} = 10^3$ J kg^{-1} K^{-1}, $\rho_s = 1440$ kg m^{-3}, and $\varphi = 0.6$. The thermal properties for the cover plate are: $c_{p,co} = 386$ J kg^{-1} K^{-1}, $k_{co} = 38.4$ W m^{-1} K^{-1}, and $\rho_{co} = 8930$ kg m^{-3}. The geometric parameters are: $L_x = 0.75$ mm, $L_{xf} = 0.5$ mm, $L_{yw} = 3$ mm, $L_{yf} = 4.5$ mm, $L_y = 6$ mm, and $L_z = 50$ mm. An accommodation coefficient of $\beta = 0.1$ was used in the numerical computation. At time $t = 0$, the evaporator is at a uniform temperature T_{in}, and both the liquid and vapor velocities are zero. At $t > 0$, a heat flux $q_e = 1.5\times 10^4$ W m^{-2} is applied at the outer surface of the cover plate, and the evaporator startup begins. Heat is transferred from the cover plate to the liquid–vapor interface, and evaporation takes place at that surface. Liquid is drawn from the bottom of the wick structure, which is kept at a temperature $T_{in} = 303$ K, and flows to the liquid–vapor interface. The evaporator gradually reaches a steady state under these working conditions.

Figure 4 shows the steady-state flow vector field in the z–y plane at $x/L_x = 0.83$. Since the magnitudes of the liquid and vapor velocities are vastly different, the vector scales for each phase are given in the figure. The magnitude of the liquid velocity increases as it approaches the liquid–vapor interface, due to the x-direction flow from the region $0 < x < L_{xf}$ to the evaporation interface. The magnitude of the vapor velocity

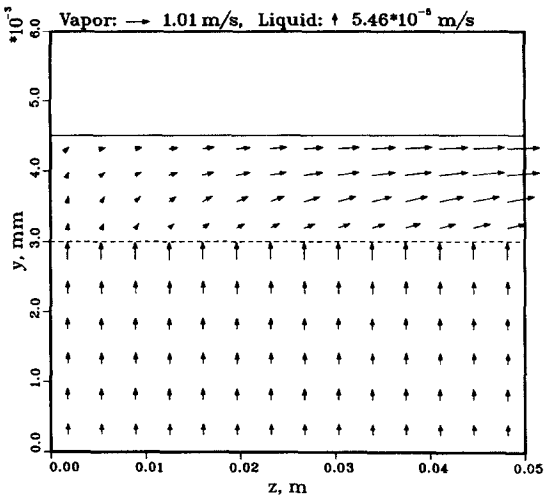

FIG. 4. Flow vectors in the porous wick structure and groove in the z–y plane at $x/L_x = 0.83$.

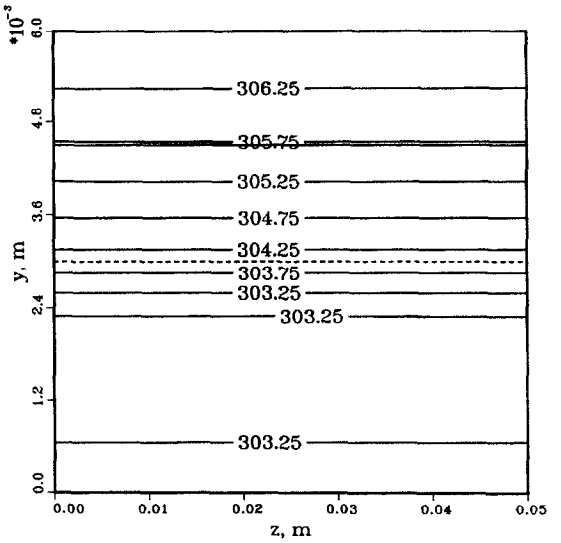

FIG. 6. Temperature contours in the z–y plane at $x/L_x = 0.83$.

increases as the vapor travels down the groove, due to the mass addition at the liquid–vapor interface. On the other hand, the liquid velocity remains constant in the z direction. Figure 5 shows the corresponding velocity vectors in the x–y plane at $z = 0.5L_z$. Liquid flow in the region $0 < x < L_{xf}$ changes direction because of the impermeable wick–cover plate interface, and flows to the wick–vapor interface. The vapor velocity at the wick–vapor interface is relatively high and gradually reduces to zero in the y direction as the evaporated vapor mass joins the main stream in the z direction, which is perpendicular to the x–y plane.

Figures 6 and 7 show the corresponding temperature contours in the z–y and x–y planes, respectively. The temperature is almost uniform in the z direction, and in the y direction it gradually increases from the inlet temperature T_{in} to the highest temperature at the outer surface of the cover plate.

Pressure drops in the wick structure and vapor groove are fairly small. For the present case, the maximum liquid pressure drop in the y direction is about 2 Pa, and that in the z direction for vapor is about 20 Pa. For a wick structure with an effective radius of the wick pores of 50 μm, for example, the maximum capillary pumping force available is on the order of 700 Pa based on equation (1). Therefore, the pressure drops in the wick and groove are very small.

After the evaporator reached the steady state, the transient pulsed performance was studied. The heat flux at the outer cover surface was suddenly increased from $q_e = 1.5 \times 10^4$ W m^{-2} to $q_e = 3 \times 10^4$ W m^{-2}. The evaporator gradually reached another steady state. Figure 8 presents the transient vapor velocities in the groove at $x/L_x = 0.83$ and $y/L_y = 0.563$ along the evaporator length for the pulsed heat input. The

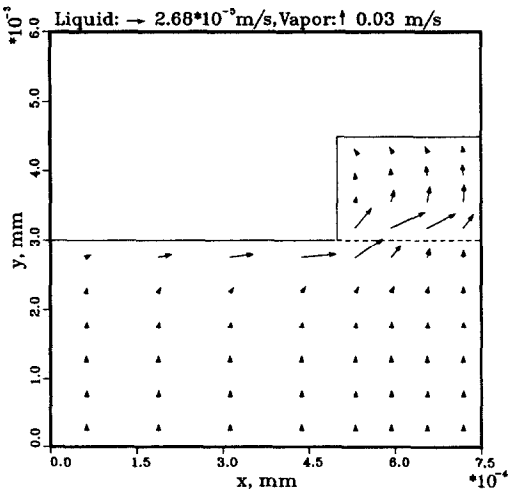

FIG. 5. Velocity vectors in the porous wick structure and groove in the x–y plane at $z = 0.5L_z$.

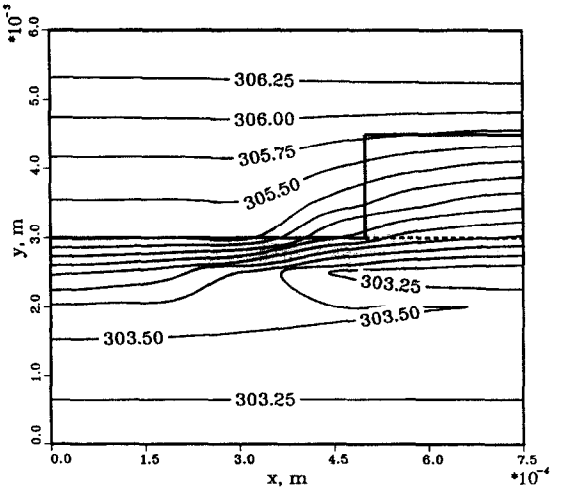

FIG. 7. Temperature contours in the x–y plane at $z = 0.5L_z$.

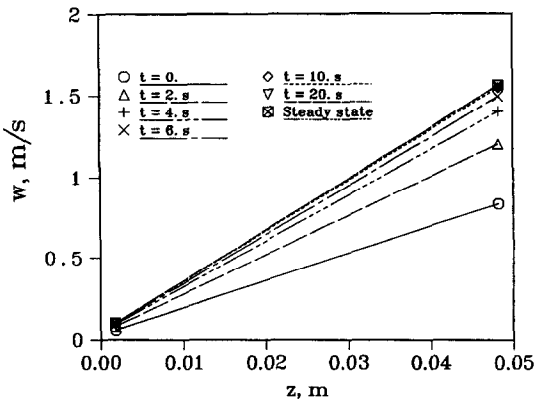

FIG. 8. Transient vapor velocities in the groove along the evaporator length for the pulsed heat input at $x/L_x = 0.83$ and $y/L_y = 0.563$.

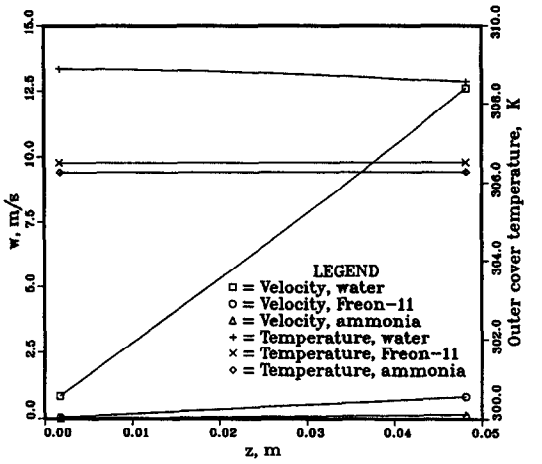

FIG. 11. Steady state vapor velocity and temperature along the evaporator length for different working fluids.

curve labeled $t = 0$ is the initial steady-state solution. As the heat input is increased, more vapor is evaporated into the groove. As a result, the vapor velocity gradually increases to a higher level. Figure 9 shows the corresponding transient vapor temperatures at the same location. Figure 10 shows the transient temperatures at the outer cover surface ($y = L_y$ and $x/L_x = 0.83$) along the evaporator length for the pulsed heat input. Compared to the vapor temperature in the groove, the outer cover temperature is relatively more sensitive to the pulsed heat input.

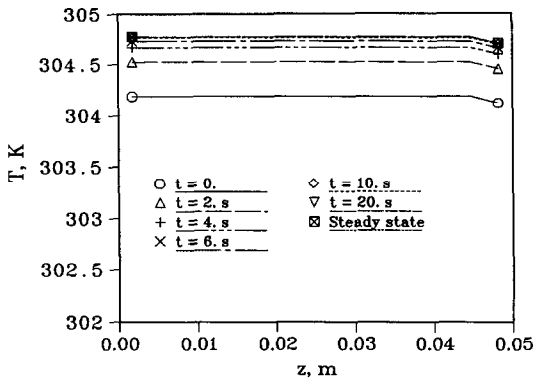

FIG. 9. Transient vapor temperature in the groove along the evaporator length for the pulsed heat input at $x/L_x = 0.83$ and $y/L_y = 0.563$.

Different working fluids were used in the computation. Figure 11 shows the steady-state vapor velocity in the groove and the temperature at the outer cover surface with $q_e = 1.5 \times 10^4$ W m^{-2} along the evaporator length for different working fluids. As can be seen, the vapor velocities for Freon-11 and ammonia are much smaller than those with water. This is mainly due to the much larger vapor densities for Freon-11 and ammonia at this working temperature. Also, the temperature for water is relatively higher than those for Freon-11 and ammonia.

It is instructive to compare the three-dimensional solutions with those of the two-dimensional model, in which the vapor flow and heat transfer in the groove were neglected, and only the solutions in the x–y plane for the porous structure and cover plate were considered. Figure 12 compares the steady-state temperatures at $x/L_x = 0.33$ and $z/L_z = 0.5$ between the

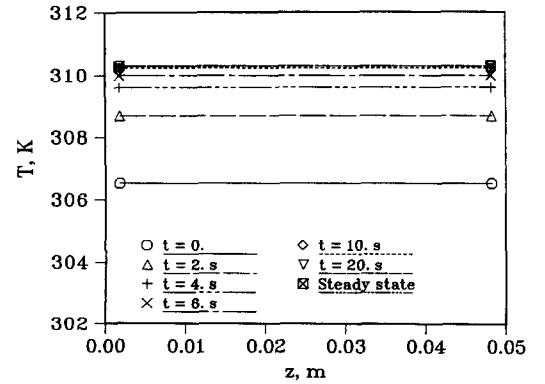

FIG. 10. Transient outer cover surface temperatures along the evaporator length for the pulsed heat input at $y = L_y$ and $x/L_x = 0.83$.

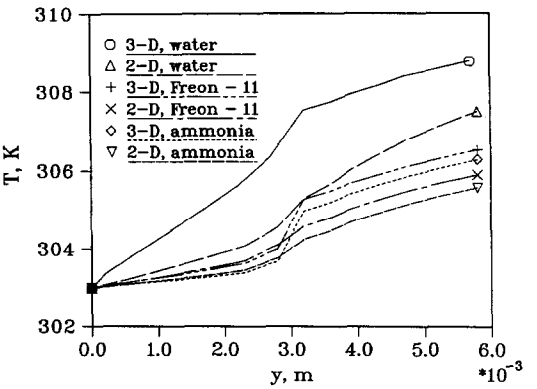

FIG. 12. Comparison between the 2-D and 3-D temperatures at $x/L_x = 0.33$ and $z/L_z = 0.5$ for different working fluids.

two- and three-dimensional models for different working fluids with $q_e = 1.5 \times 10^4$ W m^{-2}. The temperature from the three-dimensional model is generally higher than the corresponding temperature from the two-dimensional model for a given working fluid. In the two-dimensional modeling, the vapor in the groove region has not been solved, and the vapor pressure and temperature in the region remain at their initial values. Only p_l^* and T_l in equation (18) are variables in the transient operation for the calculation of mass flux $\dot{m}_\delta$. In the three-dimensional modeling, however, liquid flow in the wick structure and vapor flow in the groove region are solved simultaneously. When the heat input is applied at the evaporator, both p_v and T_v in the groove region will increase accordingly. In order to obtain the same amount of mass flux $\dot{m}_\delta$, the liquid interface temperature needs to increase to a higher level than its two-dimensional counterpart. As a result, temperatures from the three-dimensional model are generally higher than those from the two-dimensional model. The working fluid also has a strong effect on the difference between the two- and three-dimensional models. For water as the working fluid, the difference between the two models is relatively large. For Freon-11 and ammonia, however, the differences are generally small. This is attributable to the small vapor velocities for Freon-11 and ammonia as shown in Fig. 11. Although the two-dimensional modeling is less accurate than the three-dimensional model, it has the advantage of saving CPU time, and the computer coding efforts needed are much smaller.

Figure 13 shows the steady-state interface temperature and vapor velocity at $y = L_{vw}$ and $z = 0.5L_z$, with different geometric parameters for working fluid Freon-11 and heat load $q_e = 1.5 \times 10^4$ W m^{-2}. The curves labeled with case 1 are the solutions with the previous geometric parameters. For case 2, L_{wf} is changed from 0.5 to 0.375 mm. For case 3, L_{wf} is still kept at 0.5 mm, while L_{vw} is changed from 3 to 1.5 mm. It can be seen that the liquid temperature at the interface decreases in the x direction. Since the mass flux $\dot{m}_\delta$ at the evaporation interface is directly related to the liquid temperature at the interface through equation (18), the interface vapor velocities also decrease in this direction.

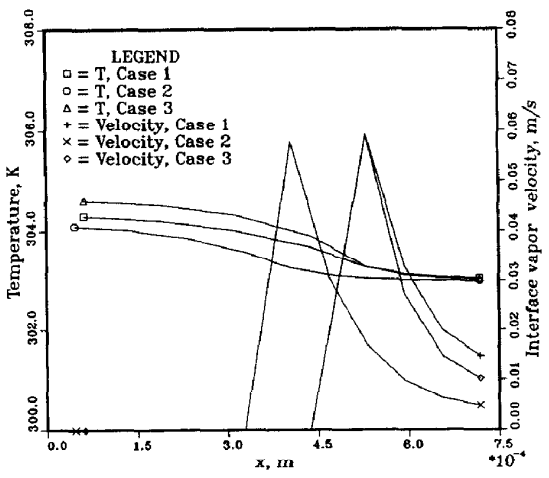

FIG. 13. Steady-state interface temperature and vapor velocity at $y = L_{vw}$ and $z = 0.5L_z$ for different geometric parameters.

CONCLUSIONS

The analysis of the evaporator performance revealed that boiling at the wick/cover-plate interface may be a major working limitation, which eliminates the capillary pumping force due to the destruction of the capillary menisci. Three-dimensional conjugate modeling shows that vapor flow in the groove is highly dependent on the working fluid used. For water, the vapor velocity is relatively high; for Freon-11 and ammonia, however, the vapor velocity is negligibly small. The pressure drops in the porous wick and the groove are also relatively small compared to the total capillary pumping force available. A two-dimensional model which neglects the vapor flow and heat transfer in the groove is compared with the more general three-dimensional model, and it is found that for some working fluids such as Freon-11 and ammonia, relatively accurate results can be obtained using the two-dimensional modeling.

REFERENCES

1. D. R. Chalmers, J. J. Pustay, C. B. Moy and E. J. Kroliczek, Application of capillary pumped loop heat transport systems to large spacecraft, *Proceedings of the AIAA/ASME 4th Joint Thermophysics and Heat Transfer Conference*, Boston, MA (June, 1986).
2. J. Ku, E. J. Kroliczek and R. McIntosh, Capillary pumped loop technology development, *Proceedings of the Sixth International Heat Pipe Conference*, France (1987).
3. H. R. Holmes, J. W. Goepp and H. W. Hewitt, Development of the Lockheed pumped two-phase thermal bus, *Proceedings of the AIAA 22nd Thermophysics Conference*, Honolulu, Hawaii (June 1987).
4. A. Kiper, G. Feric, M. Anjum and T. Swanson, Transient analysis of a capillary pumped loop heat pipe, *Proceedings of the AIAA/ASME 5th Joint Thermophysics and Heat Transfer Conference*, Seattle, WA (June 1990).
5. J. Didion and M. Martins, Two phase capillary pumped heat transfer in the instrument thermal test bed, *Proceedings of the National Heat Transfer Conference*, AIAA 92-4055, San Diego, CA (August 1992).
6. K. Furohama, K. Mimura, K. Kawamoto and K. Ohtomi, A two phase fluid loop system with multiple coldplates in parallel, *Proceedings of the AIAA/ASME 5th Joint Thermophysics and Heat Transfer Conference*, Seattle, WA (June 1990).
7. J. M. Gottschlich and R. Richter, Thermal power loops, *Proceedings of the SAE Aerospace Atlantic*, Dayton, OH (August 1990).
8. H. Wulz and E. Embacher, Capillary pumped loops for space applications experimental and theoretical studies on the performance of capillary evaporator designs, *Proceedings of the AIAA/ASME 5th Joint Thermophysics and Heat Transfer Conference*, Seattle, WA (June 1990).

9. Y. Bachmat and J. Bear, Macroscopic modeling of transport phenomena in a porous media, Parts 1 & 2, *Transport in Porous Media* **1,** 213–269 (1986).
10. E. N. Ganic, J. P. Hartnett and W. M. Rohsenow, Basic concepts of heat transfer. In *Handbook of Heat Transfer Fundamentals* (Edited by Rohsenow *et al.*). McGraw-Hill, New York (1985).
11. A. Bejan, *Convection Heat Transfer*. Wiley, New York (1984).
12. R. S. Silver and H. C. Simpson, The condensation of super-heated steam, *Proceedings of a Conference held at the National Engineering Laboratory*, Glasgow, Scotland (1961).
13. S. V. Patankar, *Numerical Heat Transfer and Fluid Flow*. McGraw-Hill, New York (1980).
14. V. S. Pratap and D. B. Spalding, Fluid flow and heat transfer in three-dimensional duct flows, *Int. J. Heat Mass Transfer* **19,** 1183–1188 (1976).